Journal of Aerosol Science 49 (2012) 32–47

Contents lists available at SciVerse ScienceDirect

Journal of Aerosol Science

journal homepage: www.elsevier.com/locate/jaerosci

Unipolar charging based, hand-held mobility spectrometer for aerosol size distribution measurement

Chaolong Qi, Pramod Kulkarni *

Centers for Disease Control and Prevention, National Institute for Occupational Safety and Health, 4676 Columbia Pkwy, MS: R7, Cincinnati, OH, 45226, USA

ARTICLE INFO

Article history:
Received 28 October 2011
Received in revised form
21 February 2012
Accepted 23 February 2012
Available online 3 March 2012

Keywords:
Nanoparticle size distribution
Aerosol mobility spectrometer
Portable aerosol instrumentation
Nanoparticle exposure

ABSTRACT

A hand-held particle size spectrometer for monitoring workplace exposure to aerosols and nanoparticles with 13 channels in the 15–630 nm has been described. The instrument uses electrical mobility-based size classification in which aerosol particles are electrically charged using a unipolar corona charger, followed by classification in a condenser-type disk classifier, and particle counting using a commercial handheld condensation particle counter (CPC; Model 3007, TSI Inc., Shoreview, MN). A unipolar charger was designed to reduce multiple charging of particles which helped extend the measurable size range. The electrical classifier, which served as a low-pass mobility filter, was operated at 2:1 sheath-to-aerosol flow ratio using a single pump inside the CPC. An inversion scheme was developed to obtain discrete size distributions from cumulative mobility distributions. The sizing accuracy was also experimentally investigated using DMA-classified, near-monodisperse particles and was found to be in the range 1.4–8.1% below 300 nm, and increased to 13.6% for 500 nm particle. Experimentally measured sizing uncertainties ranged from 78–114%. The counting uncertainties of the instrument were in the range 0.1–10.5% for typical concentration range for ambient and workplace aerosols. Size distributions of test unimodal and bimodal polydisperse aerosols measured using HPSS agreed reasonably well with that from the laboratory scanning mobility spectrometer. HPSS can be useful in many routine monitoring applications, though the measured uncertainties can be large for some applications.

Published by Elsevier Ltd.

1. Introduction

With increasing production of engineered nanomaterials for technological applications, the concerns over the exposure to these nanoparticles in the workplace and the environment are growing (The National Nanotechnology Initiative, 2006). Recent toxicological studies in laboratory animals have shown adverse lung effects from exposure to low concentrations of nanomaterials such as single-walled and multi-walled carbon nanotubes, including pulmonary inflammation and rapidly developing, persistent fibrosis (Lam et al., 2004; Shvedova et al., 2005; Muller et al., 2005; Oberdörster et al., 2007; Ryman-Rasmussen et al., 2009). However, epidemiological data linking occupational exposure of nanomaterials to their possible health effects are lacking. Although the emergence of nanomaterial manufacturing is relatively new, a major obstacle for gathering such long-term exposure data has been lack of suitable portable or personal instrumentation that can simultaneously monitor different dose metrics in real time (Maynard & Kuempel, 2005; Maynard et al., 2006).

* Corresponding author. Tel.: +1 513 841 4300; fax: +1 513 841 4545.
E-mail address: PSKulkarni@cdc.gov (P. Kulkarni).

0021-8502/$ - see front matter Published by Elsevier Ltd.
doi:10.1016/j.jaerosci.2012.02.005

Current regulations for the control of airborne particle pollution in the workplace are largely mass based and vary between particulate types. Although some evidence suggests that surface area or number concentration may be a more appropriate metric of toxicity, there is no consensus on this issue (Aitken et al., 2004; Oberdörster et al., 2005; Maynard et al., 2006). Given the evolving nature of nanomaterial synthesis and a wide variety in size, morphology, and functional characteristics, it is unlikely that all possible mechanisms of toxicity for such a wide range of materials could be monitored using one universal dose metric. For airborne exposures there is still insufficient evidence to preferentially choose one exposure metric over the other, and where there is uncertainty multiple metrics should preferably be measured (Aitken et al., 2004; Oberdörster et al., 2005; Maynard & Kuempel, 2005; Aitken et al., 2006). In this respect, measurement of a number-weighted particle size distribution is desirable as it allows simultaneous estimation of three exposure metrics, i.e. number, surface area, and mass concentration of aerosols.

Aerodynamic diameter has conventionally been used to characterize particle size for most environmental and occupational aerosols because inertial impaction or sedimentation are key deposition mechanisms for larger particles in the human respiratory system. However, the fate of particles below about 500 nm in diameter is mainly governed by diffusional transport and hence diffusion-equivalent diameter is a more relevant predictor of deposition in the respiratory tract. Since electrical mobility diameter is the same as the diffusion-equivalent diameter, mobility-based techniques are therefore more useful for measurement of nanoparticles.

Many commercial instruments such as the scanning mobility particle size spectrometers (e.g. SMPS, model 3936, TSI Inc., Shoreview MN; SMPS+C, GRIMM, Germany) can provide reliable measurement of particle size distribution using electrical mobility techniques. However, these instruments are primarily suitable for laboratory research; they are large, bulky, and expensive, making them unsuitable for routine exposure monitoring. In addition, these spectrometers use a radioactive source to achieve bipolar charging of aerosol sample. The stringent regulation on the use of radioactive material makes it impractical to deploy these instruments for routine field studies, particularly in many industrial environments. Sensors that are field portable, such as AeroTrak 9000 (TSI Inc., Shoreview, MN), diffusion charger (Model 2000CE; EcoChem Analytics, League City, TX), Nano-Check (1.320, GRIMM, Germany), DiSCmini (Matter Aerosol, Switzerland), and Nanotracer (Philips Electronics, UK), are semi-empirical instruments that provide only approximate and indirect measure of one or two specific particle properties; however, they do not measure the particle size distribution.

To address these critical needs, a hand-portable mobility spectrometer to allow measurement of number-weighted particle size distribution of ultrafine aerosols and nanoparticles in industrial environments is described. This paper presents the design and development of the prototype instrument, and demonstrates its utility for routine workplace measurements.

2. Hand-held particle size spectrometer (HPSS)

The key components of HPSS include a miniature unipolar corona charger, a condenser-type (i.e. precipitator type) electrical classifier, and a commercial handheld CPC (Model 3007, TSI Inc., Shoreview MN). The aerosol particles are first electrically charged by the unipolar charger, then classified according to their electrical mobility in the classifier, and subsequently counted downstream using the hand-held CPC. CPC was chosen as the detector, instead of an aerosol electrometer, due to its better accuracy, precision, and the ability to measure low particle concentrations at very small sample flow rates. Small flow rates require smaller pumps and also allow design of smaller electrical classifiers. The CPC (Model 3007; TSI Inc., Shoreview MN) used in this study has been shown to have a counting efficiency of about 90% at 17.3 nm and close to 100% for larger particles (Hämeri et al., 2002).

The scheme combining a condenser-type mobility classification with a portable CPC detector demanded the design of a charger with high charging efficiency over the entire size range of interest. At the same time, it was also necessary to minimize multiple charging, particularly of larger particles, to reduce the bias in the size distribution measurement. As a particle's electric mobility is inversely proportional to its diameter and proportional to the number of charges on it, a higher multiple charge level makes the electric mobility a weaker function of the particle diameter, especially for larger particles with their slip correction factor approaching 1. Such a weak function increases the uncertainty of particle size distribution obtained from the measured mobility distribution. A miniature, low-cost unipolar corona charger was designed and operated to impart optimum level of electrical charge to particles. The cylindrical charger, as shown in Fig. 1, is about 3.8 cm in diameter and 2.5 cm long. The flows through the charger and the classifier are driven by the native CPC pump. The design incorporates a cylindrical geometry for the aerosol flow, with the corona charging module housed in another cross-cylinder in the aerosol flow path. As a result, the charging zone and the resulting ion cloud are shielded from the direct aerosol flow leading to minimal particle loss. No bias voltage was used to drive the ions across the grounded mesh towards the aerosol flow. Design and characterization of the classifier have been discussed in an earlier publication (Lin et al., 2009). Fig. 2 shows the assembly of the key components of HPSS and demonstrates the overall portability of the instrument for workplace monitoring applications. The disk-shaped, condenser-type classifier has two inlets, one for aerosol sample flow, and the other for the sheath flow, and only one outlet, thereby allowing operation using only one pump. The separation of particles occurs based on the electrical mobility of particles; particles with mobility smaller than a certain critical mobility (Z_p^*; corresponding to a certain voltage V^* across the electrodes) escape the classification zone and the ones with higher mobility deposit on the electrode. By stepping through a series of voltages (V) and counting the

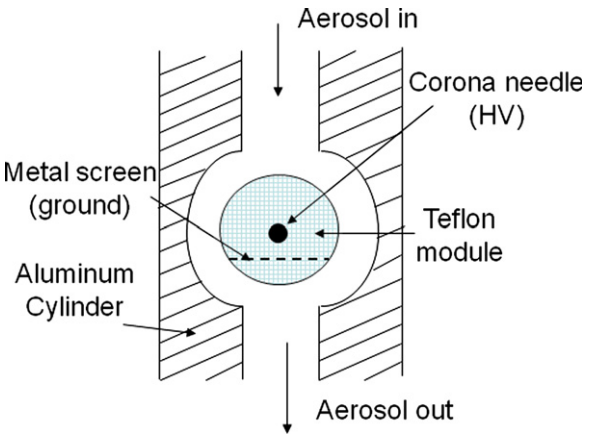

Fig. 1. Schematic diagram of the unipolar charger.

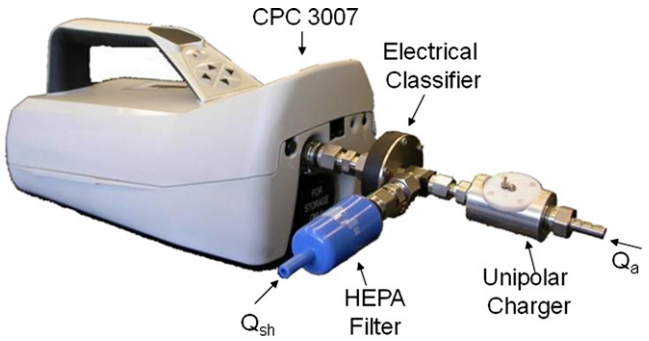

Fig. 2. Key components of the hand-held particle size spectrometer (cyclone preseparator not shown).

Table 1
Key operating parameters of HPSS.

Aerosol flow rate (l/min)	0.7
Sheath flow rate (l/min)	1.4
Size range (nm)	15–630
Number of size bins	13
Voltage range in the classifier (V)	0–3000
Time for one size distribution measurement (s)	120

number of particles penetrating the classifier, a cumulative mobility distribution can be obtained. A discrete particle size distribution is obtained by inverting the cumulative mobility distribution. The key operating parameters of the HPSS are summarized in Table 1.

Fig. 3(a) shows an overall flow scheme of the instrument. A miniature cyclone separator, with an aerodynamic cut-size of 630 nm at 0.7 lpm, is used upstream of the unipolar charger to remove larger particles from the aerosol entering the instrument. It should be noted that the miniature cyclone was not used in the laboratory experiment in this study as the laboratory test aerosols contained a negligible amount of particles larger than about 600 nm.

3. Experimental methods

3.1. Characterization of the unipolar charger and the classifier

The charging efficiency of a unipolar charger depends on the product of ion number concentration (n_{ion}) and a particle's residence time (t) in the ion cloud. Experimental characterization of the charger was performed at 0.7 l/min. The charger was operated under positive corona due its greater stability in comparison to negative corona (Hinds, 1999). A corona current of 1 μA was maintained across the electrodes in the charger to minimize the $n_{ion} \cdot t$ product and reduce the multiple charging of particles. This level of corona current also resulted in an acceptable charging efficiency as will be

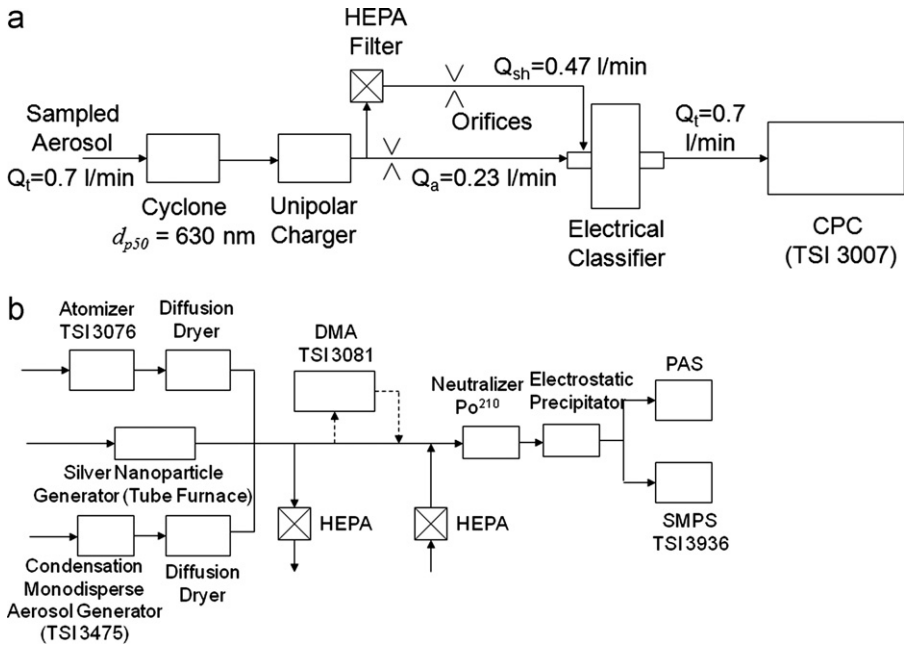

Fig. 3. Schematic illustration of: (a) flow scheme of the HPSS and (b) experimental setup used to evaluate the performance of the HPSS.

shown later. At this corona current, ozone concentration at the outlet of the unipolar charger was measured to be 22.4 ± 2.1 ppb (at 0.7 l/min). The performance of the charger was characterized using a procedure described elsewhere (Qi et al., 2007). Test aerosol for the charger was obtained by atomization of aqueous suspension of polystyrene latex (PSL) microspheres (Duke Scientific, Palo Alto, CA), followed by classification in a differential mobility analyzer (DMA, Model 3081; TSI Inc., Shoreview, MN; operating at a 10:1 sheath-to-aerosol flow ratio). The classified aerosol then passed through a Po^{210} neutralizer and an electrostatic precipitator (ESP) to provide uncharged test aerosols for the charging experiments. Experiments were designed to characterize extrinsic charging efficiency and the particle charge distribution in the particle diameter range 15–300 nm. The extrinsic charging efficiency of the charger for size d_p, $\eta_{ext}^{eff}(d_p)$ was defined as the ratio of number of particles exiting the charger with one or more unit electron charge ($N_{m\geq 1}(d_p)$, where m is unit electron charge on the particle) to the total number of particles entering the charger ($N_{tot}(d_p)$). This was obtained by measuring the concentration of neutral particles upstream and downstream of the charger. Particle charge distribution function $f_{chg}(d_p,m)$, defined as a frequency function describing the fraction of the total number of particles of size d_p carrying m charges, was obtained using tandem-DMA experiments with monodisperse PSL particles (Biskos et al., 2005). Measured $\eta_{ext}^{eff}(d_p)$and $f_{chg}(d_p,m)$ were used in the inversion of particle mobility distribution to the size distribution.

Detailed characterization and calibration of the classifier were presented in an earlier publication (Lin et al., 2009), where it was shown that a sheath-to-aerosol flow ratio of 2:1 was optimum for classifier operation. It was found that the sharpness of the cutoff curve of the classifier could not be further improved with increasing sheath-to-aerosol flow rate ratio beyond 2. Any increase of the sheath-to-aerosol flow ratio above 2 would only lower the upper size limit of the classifier without increasing the sizing resolution. The transfer function, $\Omega(Z_p^*,V)$of the classifier, defined as the fraction of particles with mobility Z_p^* penetrating the classifier at voltage V across the electrodes, is obtained by fitting the experimental transfer function data given by Lin et al. (2009):

$$\Omega(Z_p^*,V) = \frac{1.0045}{1+\exp((V/V_{50}(Z_p^*)-0.9957)/0.1290)} \tag{1}$$

where $V_{50}(Z_p^*)$ is the voltage corresponding to 50% penetration of particles with mobility Z_p^*, and can be computed from the following equation:

$$V_{50}(Z_p^*) = \frac{0.5+(Q_{sh}/Q_a)}{(\pi Z_p^*/Q_a d)(r_o^2-r_i^2)} \tag{2}$$

where, Q_{sh} and Q_a are sheath and aerosol flow rates respectively; r_o and r_i are the outer and inner radii of the bottom disk electrode of the classifier; d is distance between the disk electrodes. The above set of equations permits computation of penetration of particles with mobility Z_p^* through the classifier.

3.2. The experimental evaluation of HPSS

A slightly modified flow configuration (compared to that in Fig. 2) was used for laboratory testing of HPSS. As shown in Fig. 3(a), the total flow of 0.7 l/min was drawn through the charger and then subsequently split into an aerosol flow of 0.23 l/min and a sheath flow of 0.47 l/min. This flow scheme allows higher flow rate through the charger which helps reduce multiple charging in the charger. A miniature particulate filter was used to remove particles from the sheath air. Sheath and aerosol flows were controlled using microorifices. In the particle size range of interest (15–630 nm) particle loss in the orifice was estimated to be negligible due to very small Stokes number (less than 0.028; Chen et al., 2007). Fig. 3(b) shows experimental setup used to evaluate the performance of the prototype instrument. Experiments were performed to characterize: (i) sizing accuracy and precision of monodisperse particles, (ii) accuracy and precision of polydisperse size distribution measurement. Three types of aerosol generators were used to produce test aerosols for the experiments. A tube furnace was used as an evaporation-condensation particle generator to produce silver nanoparticles smaller than 50 nm in diameter. A pneumatic atomizer (Model 3076; TSI Inc., Shoreview, MN) with a diffusion-dryer was used to generate polydisperse NaCl particles with the geometric mean diameter ranging from 50 to 100 nm. A condensation monodisperse aerosol generator (Model 3475; TSI Inc., Shoreview MN) was used to generate di-2-ethylhexyl sebacate (DEHS) particles larger than 300 nm. Polydisperse aerosols from the generators were passed through a DMA, followed by a neutralizer and an ESP to obtain uncharged, near-monodisperse test aerosol for the prototype instrument.

Particle size distribution was obtained from the measured cumulative mobility distribution employing the data inversion procedure described later. Cumulative mobility distribution was obtained by stepping through a predetermined sequence of voltage across the classifier electrodes and recording the particle concentration measured by the CPC. Table 1 shows key operating parameters of the HPSS instrument. The measured size distribution was represented using 13 bins over the particle diameter range of 15–630 nm, which was equivalent to a resolution of 8 bins per decade of particle diameter. The number of size bins was based on the operating size resolution of the classifier (Lin et al., 2009). Increasing the number of bins beyond 13 provided no real gain in size resolution, but only increased the measurement time. As noted earlier, the miniature unipolar charger used in the HPSS was designed to provide optimum level of electrical charge to particles of the desired size range. The lower size limit of 15 nm was based on the acceptable level of charging efficiency of the unipolar charger. The charging efficiency below this size was considered too poor to yield reliable particle size measurements. The higher size limit was set to 630 nm to limit the large measurement uncertainty from multiple charging of larger particles. The results, from both experiment and simulation, discussed later, demonstrated that measurement accuracy and uncertainty in this size range was acceptable. It should be noted that the 630 nm upper size limit here is somewhat arbitrary (i.e., we could have set it at, say, 600 or 650 nm). We use 630 nm as it coincides with the upper limit of the size bin of the binning system described above, and is convenient to use. The particle size range, geometric mean size, and electrical mobility for each bin are provided in Table 2.

The instrument was operated in voltage stepping mode using 11 predetermined voltage steps. The classifier voltage for step 1 was set to 0 to allow measurement of total particle number concentration entering the classifier. The voltage for steps 2–10 were calculated using Eq. (2) to obtain V_{50}, corresponding to the lower bin boundaries in Table 2, assuming unit electrical charge on the particle. For the last step (i.e. step 11), the voltage was set to 3000 V to stay below the dielectric breakdown limit in the classifier. Table 3 shows voltage levels as a function of time used in the classifier operation.

To test the sizing accuracy of HPSS measurements, DMA-classified aerosols were generated in the size range of 20–500 nm by employing a combination of above aerosol generation techniques. As noted earlier, voltage-stepping yields a cumulative mobility distribution which is subsequently converted to a discrete particle size distribution using inversion routines discussed later. A lognormal distribution was fitted to the inverted particle size distribution and its geometric

Table 2
Boundaries, geometric mean diameter, and the mean electrical mobility of each size bin of the HPSS.

Number of size bin	Bin boundaries (nm)	Bin center, d_{pm} (nm)	Central electrical mobility of bin, Z_{pm} (cm^2/V s)
1	15.00–20.00	17.32	7.60E−03
2	20.00–26.67	23.10	4.32E−03
3	26.67–35.57	30.80	2.47E−03
4	35.57–47.43	41.08	1.42E−03
5	47.43–63.25	54.78	8.26E−04
6	63.25–84.35	73.05	4.85E−04
7	84.35–112.48	97.41	2.90E−04
8	112.48–150.00	129.89	1.76E−04
9	150.00–200.03	173.22	1.10E−04
10	200.03–266.74	230.99	7.07E−05
11	266.74–355.71	308.03	4.67E−05
12	355.71–474.34	410.76	3.17E−05
13	474.34–632.54	547.76	2.20E−05

Table 3
Time sequence of voltage application in the electrical classifier.

Sequential time, s	Voltage (V)
0–10	0
10–20	29
20–30	51
30–40	89
40–50	155
50–60	269
60–70	460
70–80	778
80–90	1290
90–100	2093
100–110	3000

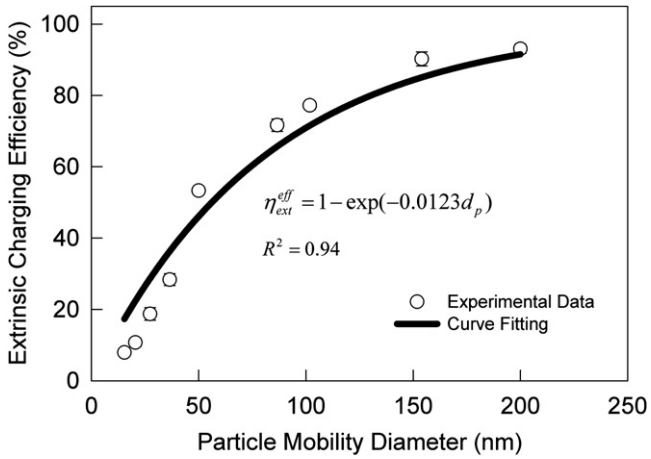

Fig. 4. Extrinsic charging efficiency of the unipolar charger.

mean diameter was obtained as a measure of mean response diameter. The measured or response diameter was compared with the known input particle diameter (DMA centroid diameter at a given voltage) to evaluate sizing accuracy of HPSS.

The instrument was also tested using unimodal polydisperse aerosols with geometric mean diameter d_{pg} ranging from 25 to 100 nm and geometric standard deviation σ_g ranging from 1.3 to 1.8. A test aerosol with bimodal size distribution was also used and was obtained by mixing the silver nanoparticles from the tube furnace with the NaCl particles from the pneumatic atomizer.

Total number concentration of the test aerosols in all the experiments ranged from about 50 to 10^5 cm^{-3}. Experiments were also performed to compare the total number concentration obtained by integrating the inverted size distribution measured by HPSS to that directly measured by a reference CPC (TSI Inc., Shoreview MN, Model 3025A).

4. Results and discussions

4.1. Characterization of unipolar charger

Experiments were conducted to obtain the extrinsic charging efficiency $\eta_{ext}^{eff}(d_p)$ of the unipolar charger as a function of particle mobility diameter. As shown in Fig. 4, the lowest charging efficiency was about 7.9% for 15 nm particles, increasing gradually to about 80% for 100 nm particles. For larger particles the charging efficiency was close to 100%. The best fit could be described by the equation $\eta_{ext}^{eff} = 1 - e^{-0.0123 d_p}$, which had an R^2 value of 0.94.

The extrinsic charging efficiency was lower compared to other unipolar chargers (Qi, et al., 2007, 2008) due to lower $n_{ion} \cdot t$ product. In order to reduce multiple charging of larger particles, the $n_{ion} \cdot t$ product was intentionally kept lower. However, an undesirable effect of low $n_{ion} \cdot t$ product and the resulting lower charging efficiency is larger measurement uncertainty, particularly at small particle sizes where counting efficiency of the CPC is low. As noted earlier, to limit the measurement uncertainty, the lower size limit of the HPSS was set to 15 nm, where η_{ext}^{eff} was 7.9%. As will be evident later, this charging efficiency at this lower size limit was adequate for making reliable size measurements.

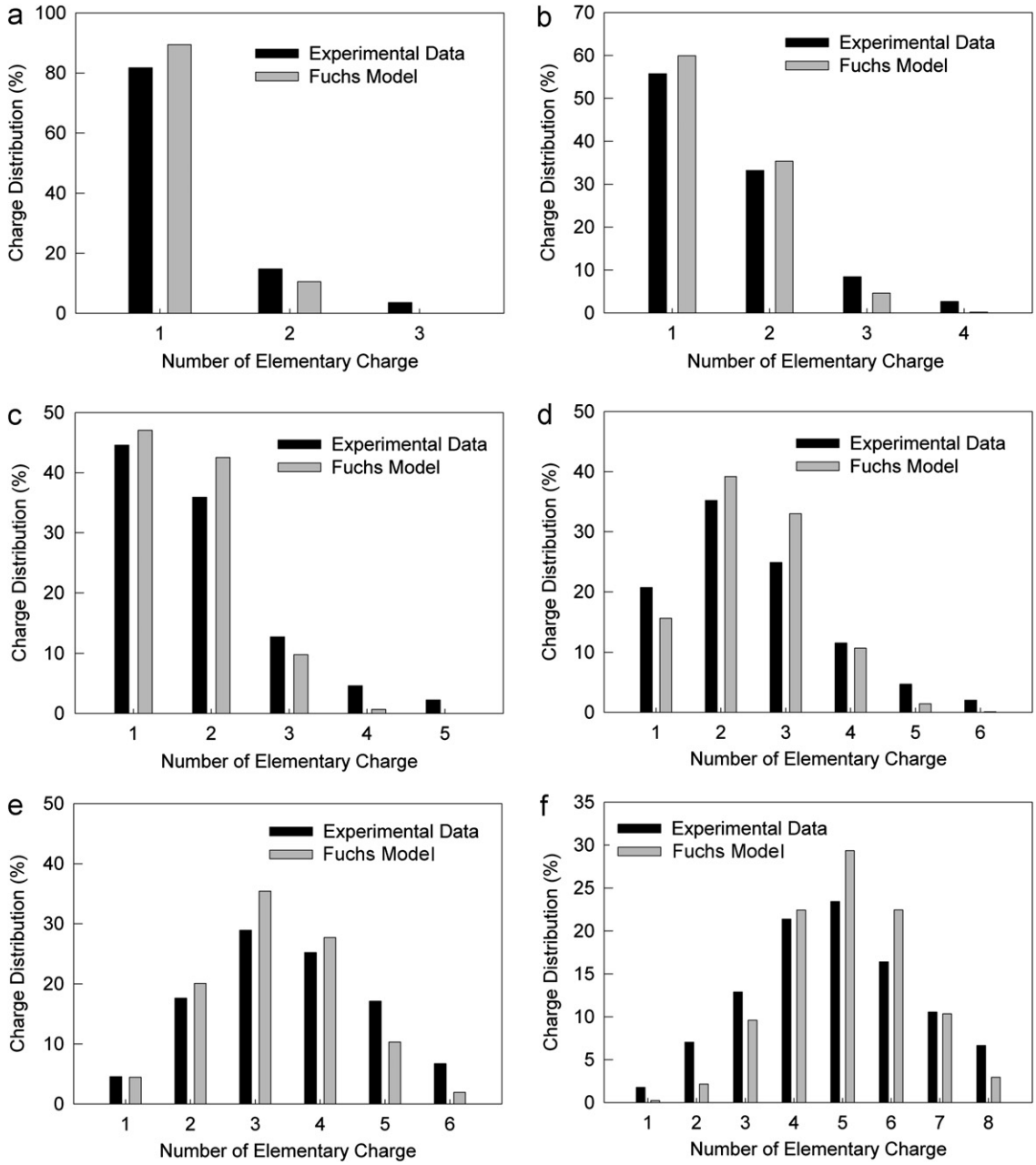

Fig. 5. The particle charge distribution of the miniature unipolar corona charger in the HPSS: (a) 50 nm, (b) 87 nm, (c) 102 nm, (d) 154 nm, (e) 202 nm, and (f) 300 nm.

Charge distribution of particles in the size range 50–300 nm exiting the unipolar charger was also obtained and shown in Fig. 5. As evident in Fig. 5, the majority of charged particles smaller than 100 nm were singly charged. Mean electrical charge on larger particles was more than 1, being equal to 2.47 for 154 nm, 3.53 for 202 nm, and 4.82 for 300 nm. The level of multiple charging was much lower compared to other unipolar chargers (Biskos et al., 2005; Qi et al., 2008). A birth-and-death model (subsequently called "Fuchs numerical model") proposed by Boisdron and Brock (1970) and using Fuchs' limiting sphere charging theory (Fuchs, 1963) has been widely used to describe diffusion charging (Adachi et al., 1985; Biskos et al., 2005). An 'apparent' $n_{ion} \cdot t$ was first derived from fitting the above Fuchs numerical model to the experimentally obtained charging data from our charger, by treating $n_{ion} \cdot t$ as a fitting parameter (see for example, McMurry et al., 2009). This approach leads to charge distributions that are 'physically realistic'. Even if, the actual $n_{ion} \cdot t$ of charger, or the distribution thereof, is different from the 'apparent' $n_{ion} \cdot t$ used in the Fuchs model, it still produces charge distributions consistent with the underlying physics of particle charging. In this study, by performing a nonlinear least squares regression between the Fuchs numerical model for unipolar diffusion charging and the experimental charge

distribution data, with $n_{ion} \cdot t$ as a free parameter, we deduced an $n_{ion} \cdot t$ value of 2.0×10^6 s cm^{-3}. Using the resulting apparent $n_{ion} \cdot t$ product, charge distributions were obtained using the Fuchs model and also plotted in Fig. 5. The agreement between the experimentally measured values and those obtained from the apparent $n_{ion} \cdot t$ was found to be reasonable. This apparent $n_{ion} \cdot t$ was subsequently used for calculating charge distribution in the data inversion routines.

4.2. Instrument response and data inversion

Response R_i of the instrument to applied voltage V_i for an input size distribution $n(\log d_p)$ is given by

$$R_i = \int_0^\infty K_i(d_p) n(\log d_p) d\log d_p + \varepsilon_i, \quad i = 1, 2, \ldots, I, \tag{3}$$

where R_i is the instrument response at voltage step i, I is the total number of voltage steps, ε_i is instrument error in step i, and $K_i(d_p)$ is the kernel function of the HPSS. The above integral equation of the instrument response can be approximated using the rectangle rule as

$$R_i \cong \sum_{j=1}^{J} K_{ij}(d_{p_j}) n(\log d_{p_j}) \log\left(\frac{d_{p_{j+1/2}}}{d_{p_{j-1/2}}}\right) + E_i \tag{4}$$

where J is the number of size channels, d_{p_j} is the midpoint particle size of channel j, where $d_{p_{j\pm1/2}}$ are the upper and lower bounds of each channel, i.e., $d_{p_j} = \sqrt{d_{p_{j+1/2}} d_{p_{j-1/2}}}$. Neglecting the error term E_i, Eq. (4) can be written in a matrix form with I equations and J unknowns as

$$\vec{R} = \Gamma \vec{n} \tag{5}$$

where $\vec{R}$ is an $I \times 1$ vector containing an array of R_i, $\vec{n}$ is a $J \times 1$ vector, representing the solution elements, $n_j = n(\log d_{p_j})$, and Γ is a $I \times J$ matrix, defined as

$$\Gamma_{ij} = K_{ij} \log\left(\frac{d_{p_{j+1/2}}}{d_{p_{j-1/2}}}\right) \tag{6}$$

A more generalized kernel function $K_{ij}(d_{p_j})$ is defined as the probability of counting particles of size d_{p_j} corresponding to size channel j in step i, and is given by

$$K_{ij}(d_{p_j}) = \left[\sum_{m=1}^{M} f_{chg}(d_{p_j}, m) \Omega(Z_p(d_{p_j}, m), V_i)\right] \eta_{CPC}(d_{p_j}) \eta_{diff}(d_{p_j}) \tag{7}$$

where $\eta_{CPC}(d_{p_j})$ is the counting efficiency of the CPC for particles of diameter d_{p_j}. Since the particle loss in the unipolar charger and the classifier are included in $f_{chg}(d_{p_j}, m)$ and $\Omega(Z_p(d_{p_j}, m), V_i)$ respectively, $\eta_{diff}(d_{p_j})$ mainly accounts for the diffusional particle loss in the plumbing connecting different components of HPSS. With the short length, the diffusional particle loss is negligible over the size range and flow rates of interest; thus $\eta_{diff}(d_{p_j})$ was set as a unit matrix in the inversion routine. The counting efficiency of the CPC has been shown to be about 90% at 17.3 nm and close to 100% for larger particles (Hämeri et al., 2002); accordingly $\eta_{CPC}(d_{p_j})$ was set to 0.9 for the first bin and 1.0 for the remaining bins in the data inversion. $f_{chg}(d_{p_j}, m)$, is the charge distribution function defined as the probability of a particle with charge level m being counted in size bin d_{p_j}. m denotes the unit charge level and can vary from 1 to M. $\Omega(Z_p(d_{p_j}, m), V_i)$ is the transfer function of the classifier as described by Eq. (1) at classifier voltage V_i for mobility $Z_p(d_{p_j}, m)$. Thus, the kernel function, K_{ij}, represents the fraction of particles with diameter d_{p_j}, that reach the detector corresponding to voltage V_i in the classifier.

In order to generate a number-weighted discrete size distribution the difference in two successive R_i is desired; therefore the differential response r_i is given by

$$r_i = R_{i+1} - R_i = (\vec{\Gamma}_{i+1} - \vec{\Gamma}_i)\vec{n} = \Delta\vec{\Gamma}_i \cdot \vec{n}, \quad i = 1, 2, I-1, \tag{8}$$

where

$$\Delta\Gamma_{ij} = \left[\sum_{m=1}^{M} f_{chg}(Z_p(d_{p_j}, m))[\Omega(Z_p(d_{p_j}, m), V_{i+1}) - \Omega(Z_p(d_{p_j}, m), V_i)]\right] \eta_{CPC}(d_{p_j}) \eta_{diff}(d_{p_j}) \log\left(\frac{d_{p_{j+1/2}}}{d_{p_{j-1/2}}}\right) \tag{9}$$

The above system of equations can be represented in the matrix form as

$$\vec{r} = \Delta\Gamma\vec{n} \tag{10}$$

The system now has $I-1$ equations with J unknowns. In order to improve the convergence and solution of above equations, a set of additional constraints were used. The first constraint required that the total number concentration of the aerosol, R_{tot}, measured by the detector before the beginning of voltage stepping (i.e. when $V=0$) must equal the total

number concentration from the size distribution, given by

$$R_{tot} = \sum_{j=1}^{J} \eta_{CPC}(d_{p_j})\eta_{diff}(d_{p_j})n(\log d_{p_j})\log\left(\frac{d_{p_{j+1/2}}}{d_{p_{j-1/2}}}\right) \tag{11}$$

In addition, the number concentration for the first and the last size bin was constrained to zero, i.e., $n_1 = n_J = 0$. Size bins were chosen such that particle diameter corresponding to $j=1$ and J were 2 and 1120 nm, respectively—way beyond the expected size range of interest for $n(\log d_{p_j})$.

An additional regularization constraint was also used which required that the second derivative of the size distribution be zero

$$\lambda \cdot D^2\vec{n} = 0 \tag{12}$$

where $D^2\vec{n}$ is a $J \times J$ matrix representing the second derivative of $n(\log d_{p_j})$. λ is a parameter governing the smoothness of the distribution curve. Larger value of λ leads to a smoother distribution.

Combining Eqs. (10)–(12), we have $I+J+2$ equations with J unknowns. We used 10 steps in I and 22 bins in J at a resolution of 8 bins per decade; increasing the number of steps beyond these values did not affect the solution, however increased the computational and measurement time.

Particle size distribution was obtained by solution of the matrix equations with appropriate constraints, using the non-negative least square regression available in MATLAB® (Mathworks, Inc.). The inversion scheme was tested using known lognormal (unimodal and multimodal) and power law size distributions as input and then comparing with the inverted size distribution. Excellent agreement was found between input distributions and the inverted distributions in all cases (Fig. A1 of Appendix A).

4.3. Accuracy and uncertainty of measurements

The accuracy of size measurement of the instrument was experimentally evaluated by measuring the response of the instrument to a known input particle diameter. DMA-classified, monodisperse aerosol with known mobility diameter in the size range 20–500 nm were used as an input to the instrument and their size distribution was measured in HPSS. The geometric mean diameter of the measured size distribution was compared with the known input diameter d_{mob} to verify the sizing accuracy and is shown in Fig. 6. Each data point represents a mean of three measurement replicates. The error bar shows the standard deviation. The figure also shows simulated response of the instrument [obtained using Eqs. (10)–(12)] for each input diameter d_{mob}. As evident from Fig. 6(a), the overall agreement between the geometric mean diameter from HPSS and the mobility diameter from the DMA is good ($R^2 = 0.98$ and 0.97 for the experimental and simulated data respectively) with the discrepancy in the rage of 1.4–8.1% below 300 nm. However, the discrepancy becomes larger for particles larger than 300 nm; it is about 13.6% and 10.5% from the experimental and simulated data, respectively, for 500 nm particles. As shown by the error bars in Fig. 6(a), the variability of the measured diameters was generally small, except for 500 nm particles, for which it was about 14.7%.

Fig. 6(b) compares the total number concentration measured by the HPSS to that by a reference CPC operating in parallel. The total number concentration measured by the HPSS is obtained from the inverted size distribution. The R^2 value is 0.999, indicating excellent agreement between the two count measurements.

The overall uncertainty of PSD measurement in HPSS is attributed to uncertainties associated with: (i) electrical charging, (ii) mobility classification, (iii) particle counting, and (iv) the numerical inversion of mobility to size distribution. As is the case with all the corona charger-based mobility spectrometers, variation in particle morphology, gas composition, humidity, temperature, and pressure can influence the charging efficiency and add to measurement uncertainties in HPSS; however, these factors were not investigated in this study. Other key sources of uncertainties unique to our instrument, namely sizing and counting uncertainty, were investigated by conducting sensitivity analysis of PSD measurement with respect to regularization parameter used in the inversion (λ; Eq. (12)), total particle concentration of the aerosol, geometric mean diameter of the input distribution (i.e., d_{pg} of the input PSD) and the width of the input distribution (i.e. σ_g of the input PSD) using the inversion framework discussed above. The detailed methodology and result of the sensitivity analysis is presented in Appendix B. In addition, the sizing uncertainty was also experimentally measured using near-monodisperse test particles as discussed later.

With any theoretical size distribution of known d_{pg} and varying λ, N_{tot}, and σ_g, the theoretical response of the HPSS can be calculated based on Eq. (10) and then used in the inversion routine to obtain an inverted size distribution. Three metrics were used to assess the accuracy and uncertainty of the inverted size distribution: coefficient of determination R^2, normalized mean root squared bias b, and relative uncertainty represented by ε_n (see Appendix B for definition of these terms).

R^2 is a measure of 'closeness' of the inverted distribution to the known theoretical or input distribution; b denotes the bias or accuracy of measured distribution with respect to the theoretical or input distribution; whereas ε_n only reflects Poisson uncertainty associated with particle counting in the detector.

Large λ (that introduces large artificial 'smoothing' of the distribution during numerical inversion) leads to less accurate output size distributions with small R^2 and larger b, while very small λ can introduce large uncertainties (i.e. large ε_n).

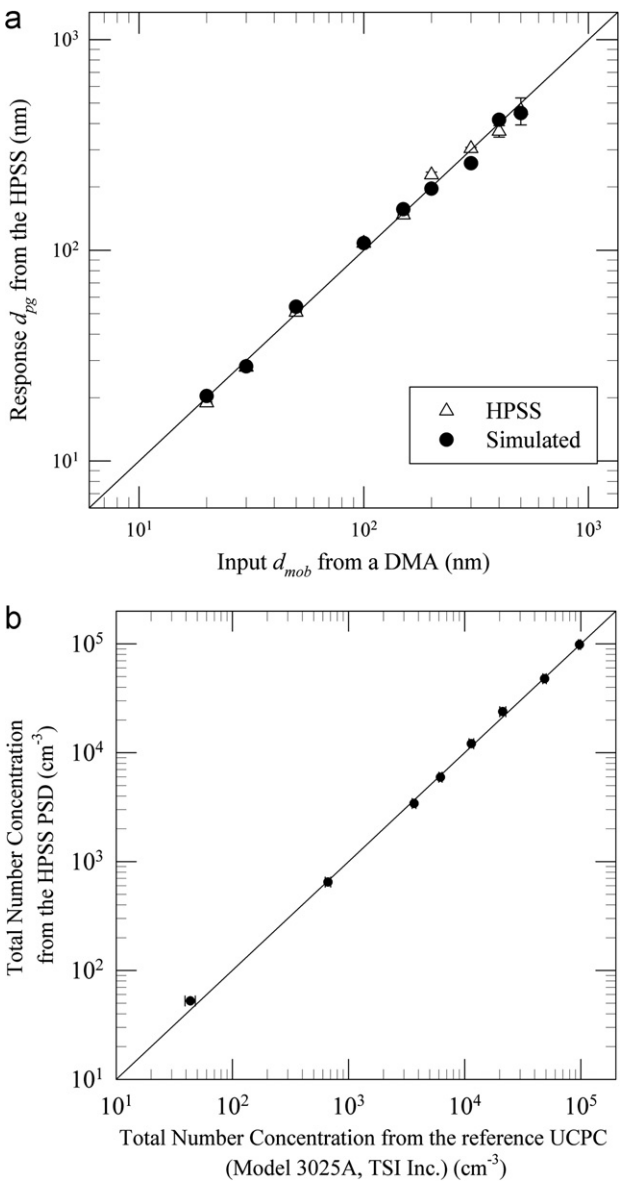

Fig. 6. The comparison of: (a) the geometric mean diameter, d_{pg}, from the particle size distribution measured by the HPSS with the input mobility diameter, d_{mob}, from a DMA and (b) total particle number concentration from the HPSS PSD and that measured by a reference UCPC (Model 3025A, TSI Inc.).

Based on our sensitivity analysis a $\lambda=0.2$ was found to give reasonable accuracy ($R^2=90\%$ or better) and no appreciable drop in the uncertainty (i.e. ε_n; Fig. B1 in Appendix B). In addition, in our instrument the uncertainty can be magnified at low number concentrations due to low aerosol flow rate through the detector (0.1 l/min). Our sensitivity analysis showed that the relative counting uncertainty of the particle size distribution, ε_n (defined by Eq. (B6) in Appendix B which reflects only Poisson uncertainty as explained earlier), can be as high as about 10% at a low particle concentrations of 100 cm^{-3} and drops down to less than 1% at high particle concentrations of 10^5 cm^{-3} (Fig. B3 in Appendix B). The degree of polydispersity also has an effect on the accuracy but its effect on ε_n is small (Fig. B4 in Appendix B). Narrower distributions with smaller σ_g are measured with less accuracy compared to those with larger σ_g due to the low size resolution of the HPSS. For input PSD with a d_{pg} smaller than 300 nm, the sensitivity analysis reveals good accuracy of the HPSS measurement, but starts deteriorating for input d_{pg} larger than 300 nm (Fig. B5 in Appendix B). As shown in Fig. B5, the R^2 is still about 0.84 for input d_{pg} of 630 nm, which is the upper size limit of the HPSS. It appears that the input PSD with a d_{pg} about 50 nm has the lowest uncertainty. We also probed the effect of time required to measure one PSD on counting uncertainty ε_n. Shorter measurement times imply larger ε_n. Fig. B6 in Appendix B shows variation of ε_n as a function of total

Table 4
Sizing uncertainty ($\Delta d_{pg}/d_{pg}$) of the HPSS's response to monodisperse aerosols.

Particle diameter (nm)	Measured uncertainty	Simulated uncertainty	
		Accounting for multiple charging	Assuming only unit particle charge
20	0.86 ± 0.01	0.79	0.73
50	0.78 ± 0.04	0.60	0.71
100	1.03 ± 0.04	0.91	0.62
150	1.12 ± 0.11	1.06	0.64
200	1.14 ± 0.08	1.05	0.62
300	0.96 ± 0.05	0.85	–
400	1.00 ± 0.04	0.87	–
500	0.82 ± 0.04	0.77	–

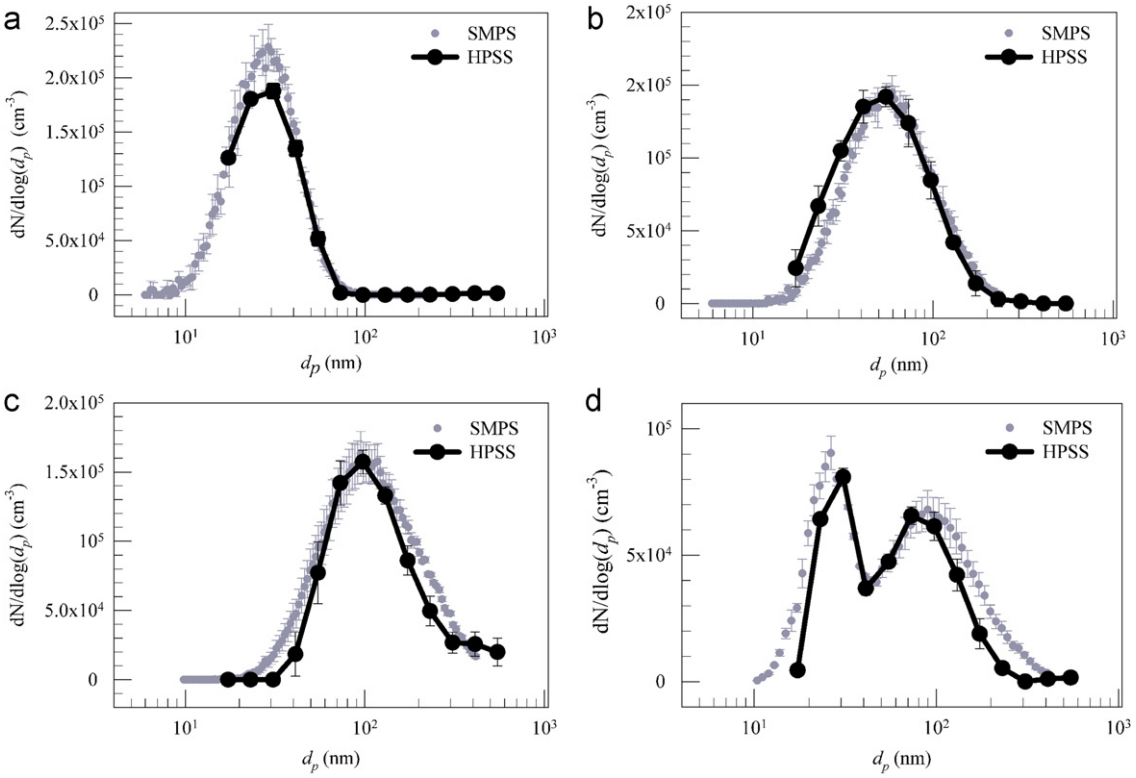

Fig. 7. Comparison of particle size distribution from SMPS and HPSS measurements: (a) unimodal with $d_{pg}=26.9$ nm, (b) unimodal with $d_{pg}=50.7$ nm, (c) unimodal with $d_{pg}=101.5$ nm, and (d) a bimodal distribution.

measurement time for one PSD. ε_n is typically less than 10%. Due to cumulative nature of mobility classification of the classifier the Poisson uncertainties are much lower than those from differential mobility classification.

In addition to sensitivity analysis, instrument's sizing resolution was experimentally investigated by measuring the response of the instrument to a known input near-monodisperse aerosol. Due to cumulative mobility classification used in our scheme, sizing uncertainty was described in terms of the 'dispersion of the inverted size distribution' of a monodisperse aerosol entering the classifier, and was defined as $\Delta d_{pg}/d_{pg}$, where d_{pg} is the geometric mean diameter obtained from the lognormal fit to the measured size distribution for near-monodisperse input aerosols, and Δd_{pg} is the full width at half maximum (fwhm) of the same distribution. Here it is assumed that the uncertainty ($\Delta d_{pg}/d_{pg}$) mainly comes from the sharpness characteristic of the cut-off curve of the electrical classifier (in addition to some numerical uncertainties in the inversion discussed above) and neglects finite size resolution of the DMA (used for generating monodisperse test aerosol). Measured and theoretically simulated uncertainties ($\Delta d_{pg}/d_{pg}$) for different input particle diameters are shown in Table 4. Note that there is no systematic trend as a function of size (though uncertainties monotonically increase with particle size below 200 nm). This is attributed to the finite binning of the size distribution and

Table 5
Comparison of HPSS and SMPS size distribution measurements.

	SMPS			HPSS		
	N_{tot} (cm^{-3})	d_{pg} (nm)	σ_g	N_{tot} (cm^{-3})	d_{pg} (nm)	σ_g
Unimodal	2.39×10^5	27.4	1.52	2.20×10^5	26.9	1.56
Unimodal	1.99×10^5	56.8	1.74	2.20×10^5	50.7	1.82
Unimodal	2.47×10^5	105.1	1.88	2.03×10^5	101.5	1.67
Bimodal						
First mode	2.45×10^4	26.0	1.33	1.82×10^4	31.5	1.18
Second mode	4.32×10^4	96.0	1.82	3.54×10^4	92.2	1.62

nonlinear contribution of uncertainties from Brownian diffusion and multiple charging as a function of size. As seen in the table, the sizing uncertainties are generally large which is attributed mainly to the low sheath-to-aerosol flow ratio in our classifier (2:1, compared to typical 10:1 used in the DMA operation). Experimental values are larger than the simulated uncertainties due to Brownian diffusion at smaller diameters and due to multiple charging at larger particle diameters.

Experiments were also performed to characterize response of the instrument to unimodal and bimodal polydisperse size distributions. Measured HPSS distributions were compared with those from the SMPS operating in parallel at an aerosol-to-sheath flow ratio of 1:10. Fig. 7 compares four distributions, unimodal distributions with geometric mean diameter (d_{pg}) of 30, 50, and 100 nm as well as a bimodal distribution. Data shown in each panel of Fig. 7 represents the averages over three replicate measurements. In order to quantitatively compare the size distributions, we used lognormal fits (described in terms of total number concentration N_{tot}, the number weighted geometric mean diameter d_{pg}, and the geometric standard deviation σ_g) to describe these distributions. The values of N_{tot}, d_{pg} and σ_g are listed in Table 5. As seen in the table, the agreement between the two instruments was good, with the values of d_{pg} and σ_g agreeing within approximately 10% of each other. It is worth noting that in spite of low charging efficiency of our unipolar charger below 100 nm, there is a good agreement in the measured size distributions in this size range.

5. Conclusion

This study indicates the usefulness of the simple scheme for measurement of nanoparticle size distributions in the indoor and work environments. Simplicity and portability are its key features. The measurement scheme can capture some key characteristics of typical aerosol size distributions; however, the size resolution can be too poor for some measurement applications, though, perhaps largely adequate for many routine applications. The multiple charging of larger particles in the unipolar corona charger can also lead to rather large measurement uncertainties.

Acknowledgments

Authors would like to thank Dr. Stanley Shulman of NIOSH for helpful discussion on uncertainty and accuracy analysis of PSD measurements.

Appendix A. The comparison of the inverted particle size distributions with the input distributions

See Fig. A1(a) and (b).

Appendix B. Investigation of measurement accuracy and uncertainty

We conducted a series of simulation tests of the data inversion scheme using different inputs of unimodal lognormal particle size distributions. The total number concentration of the input particle size distributions was varied from $10^2\ cm^{-3}$ to $10^5\ cm^{-3}$; the geometric mean diameter was varied from 20 nm to 632 nm; and the geometric standard deviation was varied from 1.1 to 2.5. For each case, the entire input and inverted size distributions, i.e., $n_{in}(\log d_{p_j})$ and $n(\log d_{p_j})$ (i.e. the inverted or output distribution) were compared using R^2. R^2 was defined as

$$R^2 = 1-\frac{\sum_j (n_{in}(\log d_{p_j})-n(\log d_{p_j}))^2}{\sum_j (n_{in}(\log d_{p_j})-\overline{n}_{in}(\log d_{p_j}))^2} \tag{B1}$$

where $\overline{n}_{in}(\log d_{p_j})$ is the average value of the input size distribution data points, $n_{in}(\log d_{p_j})$ given by

$$\overline{n}_{in}(\log d_{p_j}) = \frac{\sum_1^J n_{in}(\log d_{p_j})}{J} \tag{B2}$$

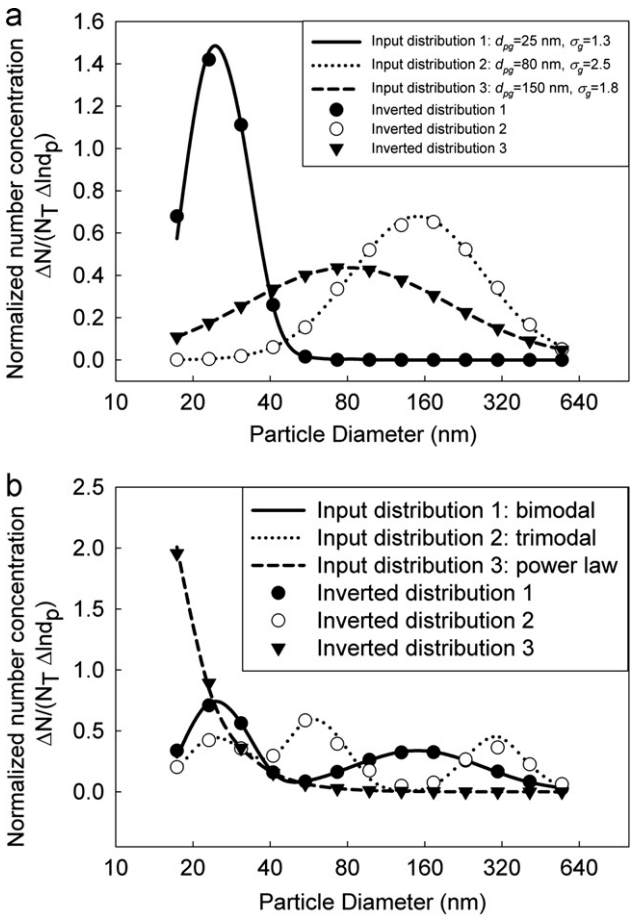

Fig. A1. The comparison of the inverted particle size distributions (obtained using the data inversion scheme of HPSS) with the input distributions: (a) unimodal lognormal distributions and (b) multimodal lognormal and power law distributions. An input size distribution was first assumed (shown by lines) and corresponding response of the instrument was calculated using Eqs. (8) and (9). The resulting response was inverted to a size distribution (shown by symbols) using inversion framework in Eqs. (10)–(12).

In addition to R^2, we also probed the measurement accuracy by using normalized bias of the PSD measurement and it is defined as

$$b = \frac{\sqrt{\sum_j (n_{in}(\log d_{p_j}) - n(\log d_{p_j}))^2}}{\sum_j n_{in}(\log d_{p_j})} \tag{B3}$$

As shown in Table 1, the CPC takes measurement for 10 s at each voltage step. The CPC measures particle concentration every one second. In the data inversion, only the data in the last 5 s of each step were used to compute the average concentration in the corresponding step (i.e. the data for the first 5 s were ignored) to ensure steady state concentration measurement. Thus, the response uncertainty is the square root of the total particle number counted in 5 s. Higher the particle concentration, lower the response uncertainty for the HPSS.

Poisson uncertainty (Δr_i) in differential response r_i, for each step i, was calculated using the following equation:

$$\Delta r_i = \frac{\sqrt{(R_i + R_{i+1})Q\,\Delta t}}{Q\,\Delta t} = \sqrt{\frac{R_i + R_{i+1}}{Q\,\Delta t}}, \quad i = 1, 2, \ldots, I-1 \tag{B4}$$

where Q is the flow rate of the aerosol entering the sensing zone, i.e., 0.1 l/min in CPC 3007, and Δt is 5 s. Here it is assumed that the two successive responses (R_i and R_{i+1}) are two independent count measurements such that the total Poisson variance of $(R_{i+1} - R_i)$ is given by the sum of individual variances as reflected in Eq. (B4) above.

Following Eq. (10), $\Delta n(\log d_{p_j})$ was computed from Δr_i using the following matrix relationship, where $\Delta n(\log d_{p_j})$ represents the uncertainty in the size distribution function $n(\log d_{p_j})$

$$\Delta \vec{r} = \Delta \Gamma \Delta \vec{n} \tag{B5}$$

The overall relative uncertainty of the inverted size distribution (ε_n) was defined using the following equation:

$$\varepsilon_n = \frac{\sum_{j=1}^{J} \Delta n(\log d_{p_j})}{\sum_{j=1}^{J} n(\log d_{p_j})} \tag{B6}$$

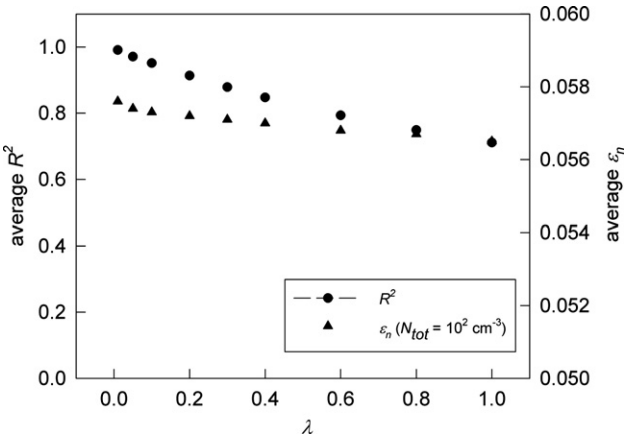

Fig. B1. Effect of regularization parameter on R^2 and ε_n of the inverted size distributions.

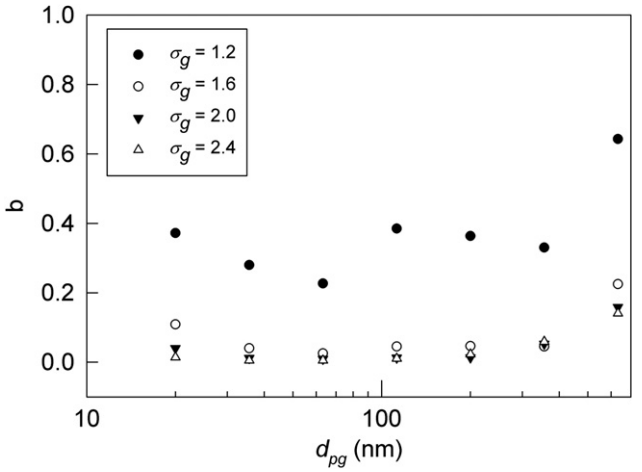

Fig. B2. Normalized bias of the PSD measurement for different input test PSDs.

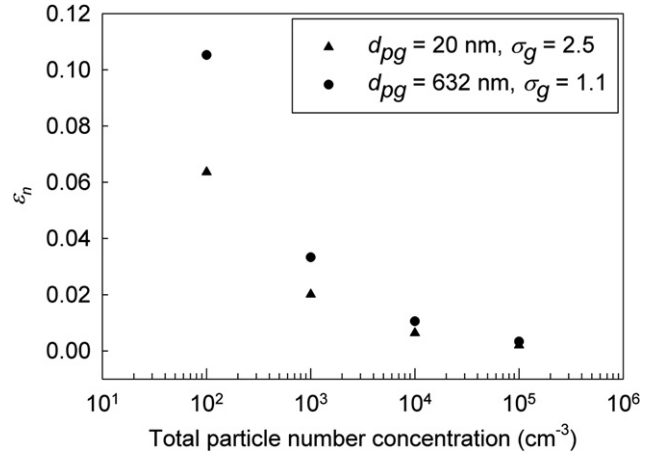

Fig. B3. Measurement uncertainty ε_n as a function of total particle number concentration of the input size distribution.

It should be noted that the ε_n defined above mainly reflects Poisson uncertainty associated with the particle counting.

In the simulation tests, the regularization parameter (a smoothing factor) λ was also varied between 0.01 and 1.0. The simulation shown in Fig. B1 shows that both average R^2 and ε_n (averaged over multiple test cases with varying size distribution parameters) for all the simulated cases decrease with λ. While a larger R^2 and a smaller ε_n are desirable, an

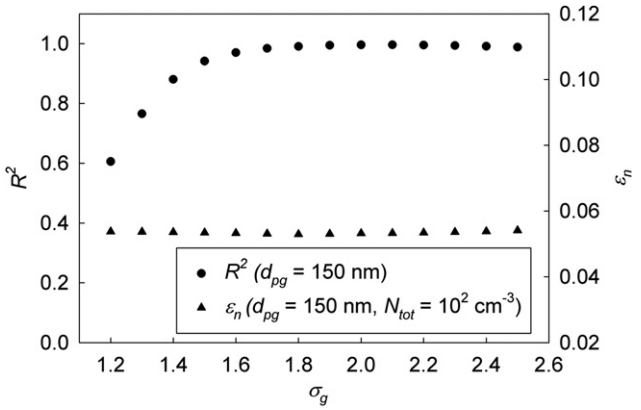

Fig. B4. R^2 and ε_n as a function of geometric standard deviation (σ_g) of the input size distribution.

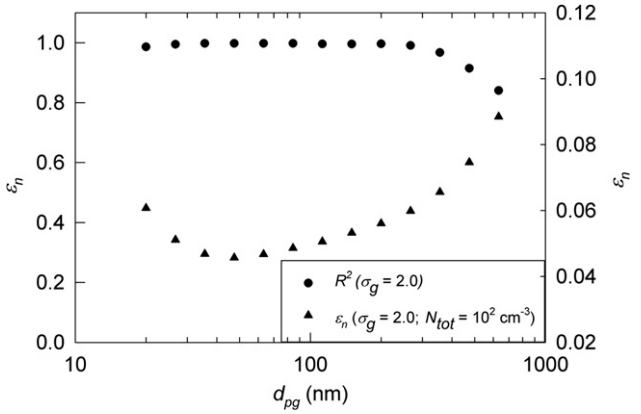

Fig. B5. R^2 and ε_n as a function of geometric mean diameter of the input size distribution.

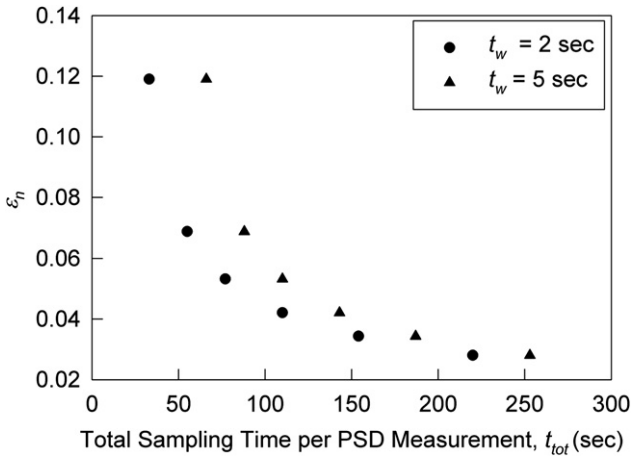

Fig. B6. Poisson measurement uncertainty ε_n as a function of total sampling time per PSD measurement. Following size distribution parameters were assumed in the simulations: $N_{tot}=10^2$ cm^{-3}, $d_{pg}=150$ nm, $\sigma_g=2.0$. t_w is the wait time (in seconds) at each voltage step required to reach steady state conditions after which the concentration measurement is recorded by the CPC. Two wait times of 2 and 5 s are shown in the above figures.

optimal λ was determined to be 0.2, since larger values did not yield significant improvement in uncertainty, however did reduce R^2 considerably. The regularization parameter λ was set to be 0.2 in all the data inversion used in this work.

The simulation results for the normalized root-mean-square bias are plotted in Fig. B2.

With the regularization parameter λ set to 0.2, the effect of the total number concentration (N_{tot}) and the geometric standard deviation (σ_g) of the input size distribution on the HPSS's measurement uncertainty was studied. As shown in Fig. B3, the magnitude of the measurement uncertainty, i.e., ε_n, significantly reduces with the increase of the total number concentration of the sampled aerosol. This is expected from Eqs. (B4) to (B6). Figs. B4–B5 show the effect of geometric mean diameter and standard deviation on the uncertainty. Fig. B6 shows the effect of sampling time per PSD.

References

Adachi, M., Kousaka, Y., & Okuyama, K. (1985). Unipolar and bipolar diffusion charging of ultrafine aerosol particles. *Journal of Aerosol Science*, *16*(2), 109–122.

Aitken, R.J., Chaudhry, M.Q., Boxall, A.B.A., & Hull, M. (2006). Manufacture and use of nanomaterials: current status in the UK and global trends. *Occupational Medicine—Oxford*, *56*, 300–306.

Aitken, R.J., Creely, K.S., & Tran, C.L. (2004). *Nanoparticles: an occupational hygiene review*. Institute of Occupational Medicine.

Biskos, G., Reavell, K., & Collings, N. (2005). Unipolar diffusion charging of aerosol particles in the transition regime. *Journal of Aerosol Science*, *36*, 247–265.

Boisdron, Y., & Brock, J.R. (1970). On the stochastic nature of the acquisition of electrical charge and radioactivity by aerosol particles. *Atmospheric Environment*, *4*, 35–50.

Chen, S.C., Tsai, C.J., Wu, C.H., Pui, D.Y.H., Onischuk, A.A., & Karasev, V.V. (2007). Particle loss in a critical orifice. *Journal of Aerosol Science*, *38*, 935–949.

Fuchs, N.A. (1963). On the stationary charge distribution on aerosol particles in bipolar ionic atmosphere. *Geofisica Pura Applications*, *56*, 185–193.

Hämeri, K., Koponen, I.K., Aalto, P.P., & Kulmala, M. (2002). The particle detection efficiency of the TSI-3007 condensation particle counter. *Journal of Aerosol Science*, *33*, 1463–1469.

Hinds, W.C. (1999). *Aerosol technology: properties, behavior and measurement of airborne particles* (2nd ed.). Wiley: New York.

Lam, C.W., James, J.T., McCluskey, R., & Hunter, R.L. (2004). Pulmonary toxicity of single-wall carbon nanotubes in mice 7 and 90 day after intratracheal instillation. *Toxicological Science*, *77*, 126–134.

Lin, L., Chen, D.R., Qi, C., & Kulkarni, P. (2009). A miniature disk electrostatic aerosol classifier for personal nanoparticle sizers. *Journal of Aerosol Science 40*, 982–992.

Maynard, A.D., Aitken, R.J., Butz, T., Colvin, V., Donaldson, K., Oberdörster, G., Philbert, M.A., Ryan, J., Seaton, A., Stone, V., Tinkle, S.S., Tran, L., Walker, N.J., & Warheit, D.B. (2006). Safe handling of nanotechnology. *Nature*, *444*, 267–269.

Maynard, A.D., & Kuempel, E.D. (2005). Airborne nanostructured particles and occupational health. *Journal of Nanoparticle Research*, *7*, 587–614.

McMurry, P.H., Ghimire, A., Ahn, H.K., Sakurai, H., Moore, K., Stolzenburg, M., & Smith, J.N. (2009). Sampling nanoparticles for chemical analysis by low resolution electrical mobility classification. *Environmental Science and Technology*, *43*(13), 4653–4658.

Muller, J., Huaux, F., Moreau, N., Misson, P., Heilier, J.F., & Delos, M. (2005). Respiratory toxicity of multi-wall carbon nanotubes. *Toxicology and Applied Pharmacology*, *207*, 221–231.

Oberdörster, G., Oberdörster, E., & Oberdörster, J. (2005). Nanotoxicology: an emerging discipline evolving from studies of ultrafine particles. *Environmental Health Perspective*, *113*, 823–839.

Oberdörster, G., Stone, V., & Donaldson, K. (2007). Toxicology of nanoparticles: a historical perspective. *Nanotoxicology*, *1*, 2–25.

Qi, C., Chen, D.R., & Greenberg, P. (2008). Performance study of a unipolar aerosol mini-charger for a personal nanoparticle sizer. *Journal of Aerosol Science*, *39*, 450–459.

Qi, C., Chen, D.R., & Pui, D.Y.H. (2007). Experimental study of a new corona-based unipolar aerosol charger. *Journal of Aerosol Science*, *38*, 775–792.

Ryman-Rasmussen, J.P., Tewksbury, E.W., Moss, O.R., Cesta, M.F., Wong, B.A., & Bonner, J.C. (2009). Inhaled multiwalled carbon nanotubes potentiate airway fibrosis in murine allergic asthma. *American Journal of Physiology—Lung Cellular and Molecular Physiology*, *40*, 349–358.

Shvedova, A.A., Kisin, E.R., Mercer, R., Murray, A.R., Johnson, V.J., & Potapovich, A.I. (2005). Unusual inflammatory and fibrogenic pulmonary responses to single walled carbon nanotubes in mice. *American Journal of Physiology—Lung Cellular and Molecular Physiology*, *289*, L698–L708.

The National Nanotechnology Initiative. (2006). *Environmental, health, and safety research needs for engineered nanoscale materials*, National Science and Technology Council.